RESEARCH ARTICLE

Key Points:
- Neutral winds modify the geographical distribution and character of responses in electron density, ion temperature, and electron temperature
- Neutral winds modify the lags of neutral temperature and mass density responses with respect to totality
- Comparisons with observations reveal some model deficiencies that should be addressed in future work

Correspondence to:
I. Cnossen,
inos@bas.ac.uk

The Response of the Ionosphere-Thermosphere System to the 21 August 2017 Solar Eclipse

I. Cnossen[1,2] , **A. J. Ridley[1]** , **L. P. Goncharenko[3]** , and **B. J. Harding[4]**

[1]Climate and Space Sciences and Engineering, University of Michigan, Ann Arbor, MI, USA, [2]British Antarctic Survey, Cambridge, UK, [3]MIT Haystack Observatory, Westford, MA, USA, [4]Department of Electrical and Computer Engineering, University of Illinois at Urbana-Champaign, Urbana, IL, USA

Abstract We simulated the effects of the 21 August 2017 total solar eclipse on the ionosphere-thermosphere system with the Global Ionosphere Thermosphere Model (GITM). The simulations demonstrate that the horizontal neutral wind modifies the eclipse-induced reduction in total electron content (TEC), spreading it equatorward and westward of the eclipse path. The neutral wind also affects the neutral temperature and mass density responses through advection and the vertical wind modifies them further through adiabatic heating/cooling and compositional changes. The neutral temperature response lags behind totality by about 35 min, indicating an imbalance between heating and cooling processes during the eclipse, while the ion and electron temperature responses have almost no lag, indicating they are in quasi steady state. Simulated ion temperature and vertical drift responses are weaker than observed by the Millstone Hill Incoherent Scatter Radar, while simulated reductions in electron density and temperature are stronger. The model misses the observed posteclipse enhancement in electron density, which could be due to the lack of a plasmasphere in GITM. The simulated TEC response appears too weak compared to Global Positioning System TEC measurements, but this might be because the model does not include electron content above 550-km altitude. The simulated response in the neutral wind after the eclipse is too weak compared to Fabry Perot interferometer observations in Cariri, Brazil, which suggests that GITM recovers too quickly after the eclipse. This could be related to GITM heating processes being too strong and electron densities being too high at low latitudes.

1. Introduction

On 21 August 2017, a total solar eclipse took place, casting a shadow that passed from the Pacific Ocean across the continental United States in a southeastern path to the Atlantic Ocean (e.g., Huba & Drob, 2017). The eclipse started at 15:46 and ended at 21:04 UT, with totality occurring between 16:49 and 20:02 UT. As a solar eclipse partially blocks the Sun's extreme ultraviolet (EUV) radiation, the temperature and electron density in the upper atmosphere are reduced due to decreased EUV heating and photoionization. This leads to further changes in thermosphere dynamics, which additionally interact with the ionospheric structure. For instance, thermal cooling leads to downwelling, which modifies the O/N_2 ratio, leading to changes in electron density (e.g., Müller-Wodarg et al., 1998; Wu et al., 2018). Solar eclipses therefore offer us a unique way to gain new insights in how the thermosphere-ionosphere system works, and they also provide an interesting test case for the performance of thermosphere-ionosphere models.

Here we explore the response of the ionosphere and thermosphere to the 21 August 2017 solar eclipse with the Global Ionosphere Thermosphere Model (GITM). The key two goals of this study are to (1) elucidate the mechanisms at work that are responsible for certain features of the response to the eclipse event and (2) identify which aspects of the observed responses are captured well by the model and which are not, and to understand better why certain aspects are not captured well. This information can then be used to make further model improvements.

This paper is organized as follows. In section 2 we describe the setup of the model simulations used. Results are presented in section 3, with section 3.1 focusing on various aspects of the model results and section 3.2 focusing on comparisons with observational data sets. A discussion of the results with a summary of the main findings and conclusions is given in section 4.

2. Methodology

The GITM (Ridley et al., 2006) was used to simulate the effects of the 21 August 2017 eclipse. It was run with a resolution of 2.0° latitude by 4.0° longitude by roughly 0.3 times the scale height in altitude, and spanning from 100 km to approximately 550-km altitude. The Weimer (2005) electric potential and Newell et al. (2009) auroral precipitation patterns were used, driven by time-delayed solar wind and interplanetary magnetic field data from the Advanced Composition Explorer satellite (Stone et al., 1998). The Naval Research Laboratory Mass Spectrometer Incoherent Scatter radar model (Picone et al., 2002) was used to specify neutral densities and temperatures at the lower boundary, just below 100-km altitude, and the Horizontal Wind Model 2014 (Drob et al., 2015) was used to specify neutral winds at the lower boundary. The ions have a continuous gradient lower boundary condition. The newly updated electron, ion, and neutral temperature scheme as described by Zhu et al. (2016) was used. The Flare Irradiance Spectral Model (Chamberlin et al., 2007) was used to specify the solar EUV spectrum. The model was initialized with Naval Research Laboratory Mass Spectrometer Incoherent Scatter, Horizontal Wind Model 2014, and the International Reference Ionosphere (Bilitza et al., 2014), starting at 0 UT on 20 August 2017.

To simulate the effects of the eclipse, GITM was modified to reduce the EUV heating and ionization in the region of the moon occultation of the Earth. This was done in the same way as described by Wu et al. (2018), although they used a different EUV model. The path of the eclipse was defined in Geocentric Solar Ecliptic (GSE) coordinates as a straight line in the (Y_{GSE}, Z_{GSE}) plane, assuming X_{GSE} to remain constant. The reduction in EUV irradiance was based on the distance (r) between each GITM grid point and the center of totality: at the center of totality, the EUV irradiance at all wavelengths was reduced to 10% of the normal value, which linearly increased until the edge of the occultation region was approached, after which the EUV increased exponentially back to 100% at 3,800-km distance from the center of totality. The remaining 10% at totality is to allow for EUV radiation coming from the solar corona, which is not obscured at totality. A more detailed description of the methodology can be found in Wu et al. (2018). We compare the simulation with the eclipse EUV mask to a simulation without the mask, to assess the response of the thermosphere-ionosphere system to the eclipse as simulated by GITM.

3. Results

3.1. GITM Response to the Eclipse

As the eclipse progresses along the path of totality, the thermospheric temperature and density decrease. Figure 1 shows global maps of the temperature and winds at 400-km altitude over the course of the eclipse and for several hours afterward. At 17:00 UT, just after the start of the total eclipse, a decrease in thermospheric temperature of around 20–30 K can already be observed, more or less centered on the location of the shadow at that time. As the eclipse progresses, the reduction in temperature intensifies and starts to lag behind the shadow. The largest temperature reduction of ∼ 70 K occurs around 20–21 UT. As the temperature declines, a pressure gradient is set up, resulting in horizontal neutral winds of up to 55 m/s rushing in to fill the pressure "hole" created by the eclipse. The winds are strongest on the leading edge and sides of the occultation region and weakest on the trailing edge. After 21:00 UT, at the end of the eclipse, the temperature reduction weakens and perturbation winds slow down, though the large-scale gravity wave set up by the occultation still progresses through the atmosphere, beyond the path of the eclipse. A similar wave was simulated by Dang et al. (2018) with a high-resolution version of the Thermosphere-Ionosphere-Electrodynamics General Circulation Model (TIE-GCM).

We examine the structure of the response of various thermospheric and ionospheric variables to the eclipse in greater detail in Figures 2–4. Figure 2 shows zoomed-in maps of neutral temperature, mass density, and wind at 19 UT at 400 and 202-km altitude. We focus on the altitude of 400 km as an example throughout this section and also show results for 202-km altitude for comparison. We will comment on how the responses at 202-km altitude compare to those at 400 km at the end of section 3.1.

The eclipse-induced temperature decrease results in atmospheric contraction, which causes the thermospheric density at a fixed altitude of 400 km to decrease by up to nearly 30%. Both the neutral temperature and mass density responses lag behind the location of totality. This indicates that the thermosphere is out of thermal equilibrium in the region surrounding totality, with cooling exceeding heating, so that the temperature response continues to grow for some time after totality has passed, until the peak temperature response (i.e., the most negative value) is reached, when heating and cooling briefly balance, before heating takes
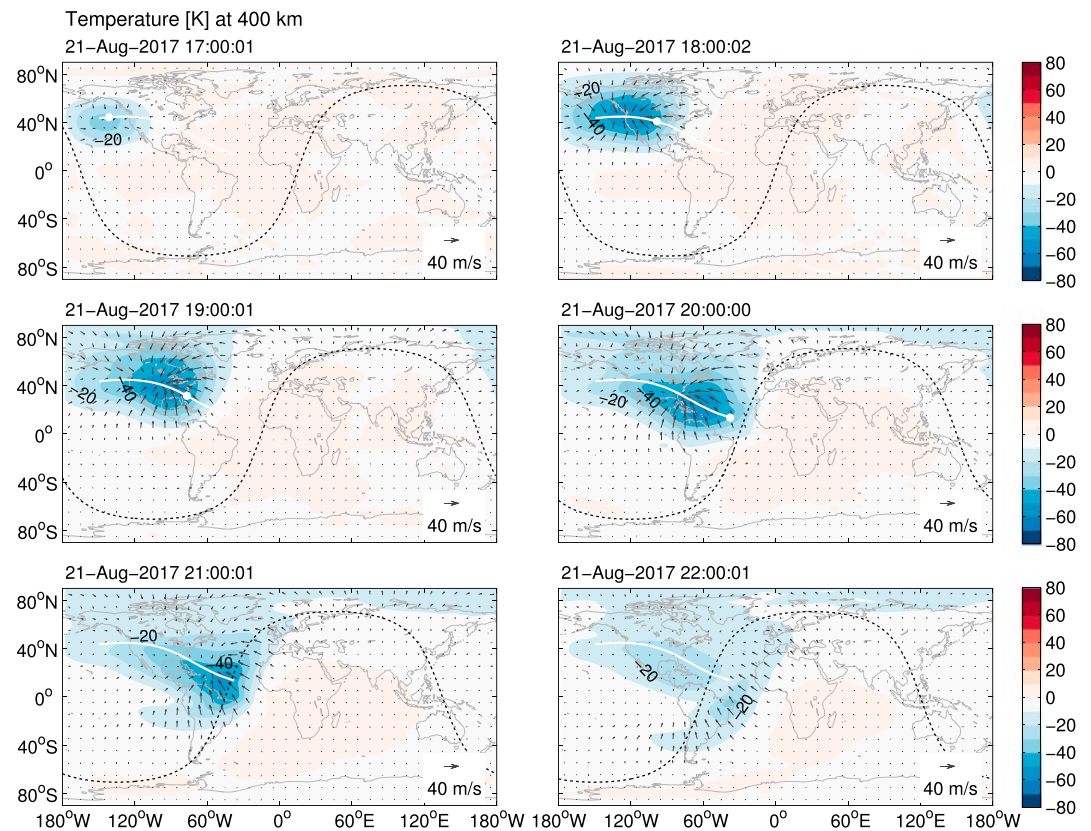
Figure 1. Response of the neutral temperature (colored contours) and horizontal wind (vectors) at 400-km altitude at 1-hr intervals from 17:00 to 22:00 on 21 August 2017. The white line marks the path of the center of totality, with the white dot indicating its current position. The dashed black line marks the location of the solar terminator.

over and the temperature is gradually restored back toward the preeclipse equilibrium. However, despite the close linkage between temperature and density, the lag of the peak temperature response with respect to totality is slightly larger than that of the peak density response (see also Figure 5). The spatial structure of the temperature and density responses show some small differences as well, although their overall structure is similar. Differences in the temperature and density responses may be caused by the neutral winds.

The horizontal winds (vectors in Figure 2e/2f) respond to the change in horizontal pressure gradient, so that they converge to the location of the pressure minimum, which is determined by a combination of the temperature and density responses. However, the perturbation winds at 400-km altitude converge toward a point further to the northwest (43°N, 102°W) from where the current temperature and density minima are located (39°N, 94°W and 33°N, 82°W, respectively). This is probably due to the time it takes for the neutral winds to adjust, while the eclipse, and therefore, the location of the pressure minimum, moves very quickly. This effect can also be seen in simulations with the TIE-GCM by Wang et al. (2019). Both the background and perturbation horizontal winds can alter the temperature and density responses through advection, but they do not necessarily affect both parameters in exactly the same way because of underlying differences in the temperature and density structures. Vertical winds can also modify the temperature and density responses through advection, but can additionally cause adiabatic heating/cooling and compositional changes that affect the mass density.

At 400-km altitude, downward perturbation winds of $\sim$ 6 m/s occur on the leading edge of the eclipse and immediately around the region of totality, while upward winds are present on the trailing edge. The vertical wind response forms as a result of changes in the vertical pressure gradient associated with the eclipse-induced cooling. As the eclipse approaches and the atmosphere cools, the vertical pressure gradient weakens, resulting in relatively more downward motion. Soon after totality has passed, the vertical pressure gradient starts to strengthen again, causing air to move up again. Downward motion causes a reduction in mean molar mass as it brings air rich in atomic oxygen down, so it acts to enhance the density reduction,
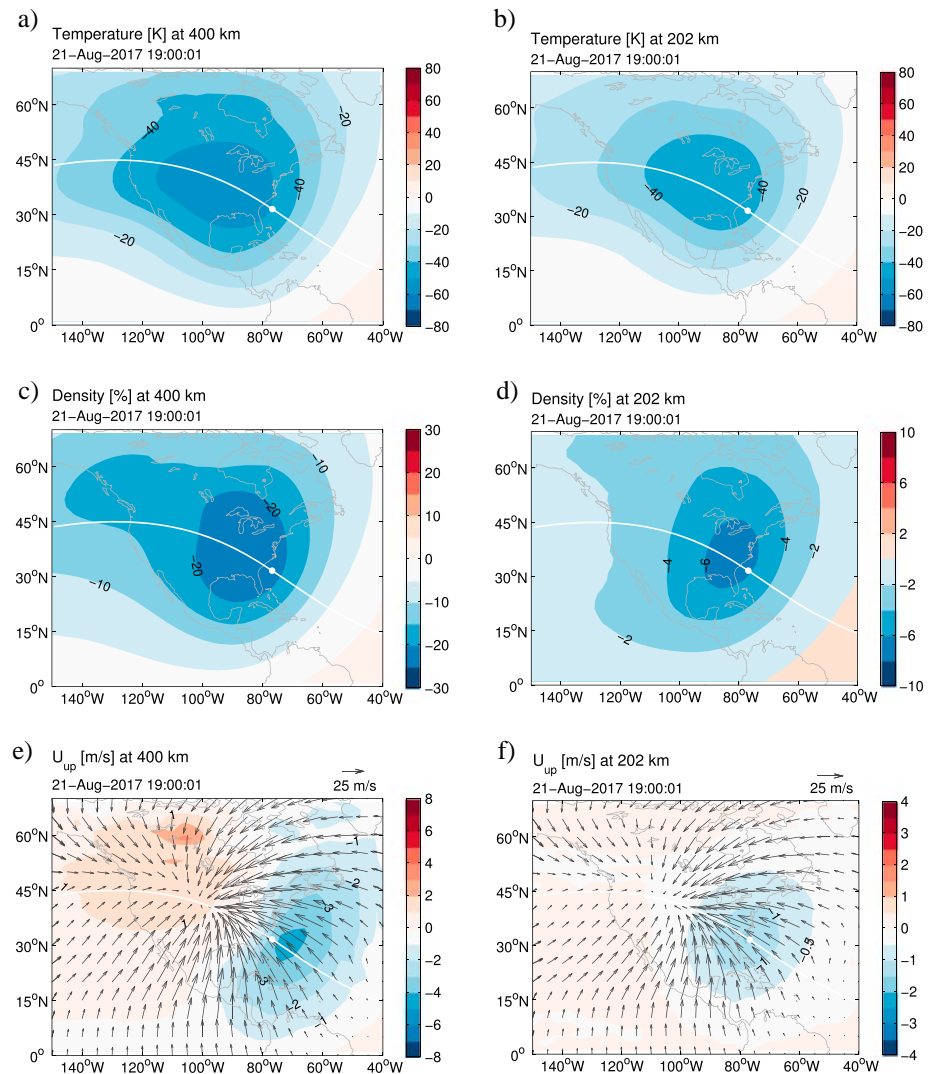
Figure 2. Response of neutral temperature (a, b), neutral density (c, d), and upward and horizontal wind (colored contours and vectors, respectively; e, f) at 400- (left column) and 202-km (right column) altitude at 19 UT on 21 August 2017. The white line marks the path of the center of totality, with the white dot indicating its current position.

while adiabatic heating associated with downwelling acts to reduce the temperature reduction. This could perhaps explain the slightly smaller lag of the peak density response with respect to totality.

Figure 3a shows a zoomed-in map of the total electron content (TEC) response at 19 UT. The reduction in TEC also lags a little behind the center of totality, and peaks at nearly 6 TECU. This is a slightly stronger reduction than previously simulated by Huba and Drob (2017) with Sami3 is Also a Model of the Ionosphere (SAMI3) and by Dang et al. (2018) with the TIE-GCM, which both showed a maximum reduction of ~5 TECU. One factor that might contribute to this difference is the slightly different eclipse masks that were used: in the simulations by Huba and Drob (2017) and Dang et al. (2018) somewhat more of the EUV radiation remained at totality, namely, 15% and 22%, respectively, whereas in our case this was only 10%. On the other hand, the totality region is very small (about the size of 1 grid cell in GITM), so the effect of this difference should be small. We also note that Huba and Drob (2017) showed fairly extensive effects in the conjugate hemisphere, which in our case were much more limited. This is probably due to GITM's upper boundary of ~ 550 km altitude, which means that magnetic field lines extending to higher altitudes are cut off, limiting interhemispheric plasma transport along the magnetic field. Other models that extend to a certain height or pressure level (e.g., the TIE-GCM) also suffer from this problem. While GITM should still be able to capture interhemispheric coupling via electrodynamical processes, we do not see a significant
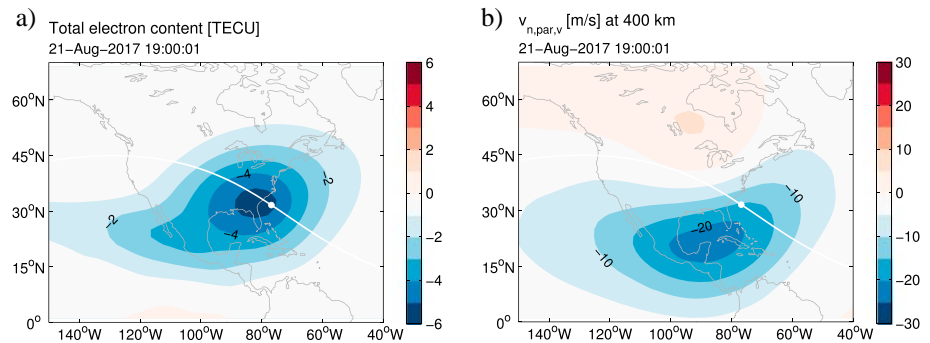
Figure 3. Response of total electron content (a) and $v_{n,par,v}$ at 400-km altitude (b) at 19 UT on 21 August 2017. The white line marks the path of the center of totality, with the white dot indicating its current position.

response in the conjugate hemisphere in our simulations. Since the main effects in our simulations occur in the region surrounding the eclipse trajectory, this is the region we will focus on here. While the peak reduction in TEC simulated by GITM is somewhat stronger than simulated by other models, it is noticeably weaker than observed in Global Navigation Satellite System data by Coster et al. (2017), which indicated reductions of up to 8 TECU at 18:32 UT. However, the shape of the simulated response, with a tail extending equatorward and westward of the path of the eclipse, was a feature also observed by Coster et al. (2017).

The equatorward and westward extension of the TEC reduction can be explained by the enhanced northward neutral winds in that region (see Figure 2e). This blows plasma down along the magnetic field equatorward of the eclipse path, into a region of higher recombination, acting to reduce the TEC. Poleward of the eclipse path, the perturbed neutral winds are weaker and act primarily in the opposite direction. The role of the neutral wind is further confirmed in Figure 3b, which shows the response of the vertical component of the projection of the horizontal neutral wind onto the magnetic field, which we refer to as $v_{n,par,v}$; this is the part of the horizontal neutral wind that contributes to the vertical plasma transport along the magnetic field. The structure of the $v_{n,par,v}$ response is similar to that of the TEC response. Since the magnetic field declination
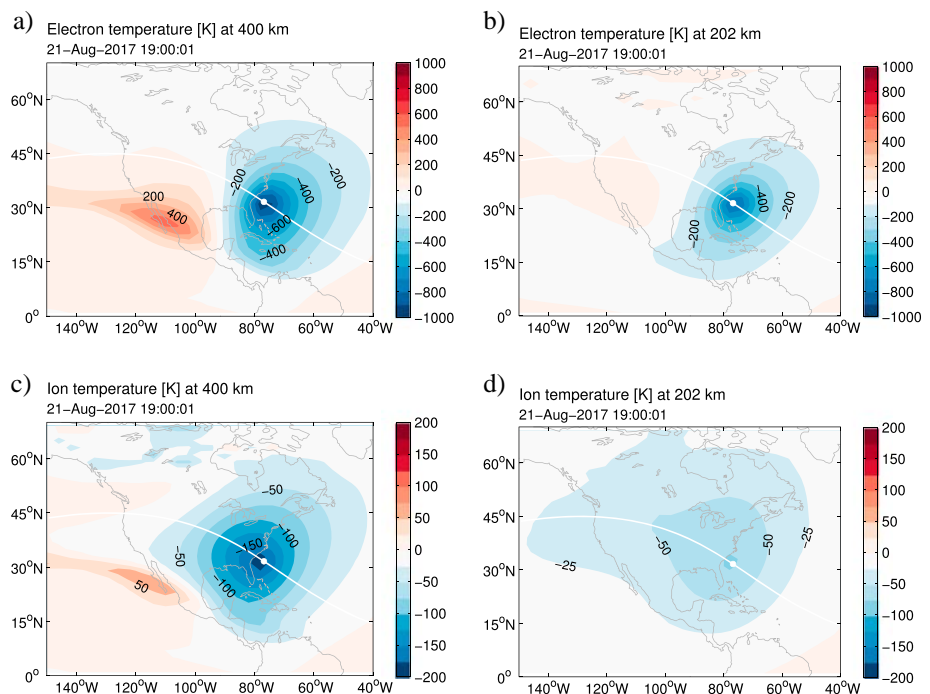

Figure 4. Response of electron temperature (a, b) and ion temperature (c, d) at 400- (left column) and 200-km (right column) altitude at 19 UT on 21 August 2017. The white line marks the path of the center of totality, with the white dot indicating its current position.
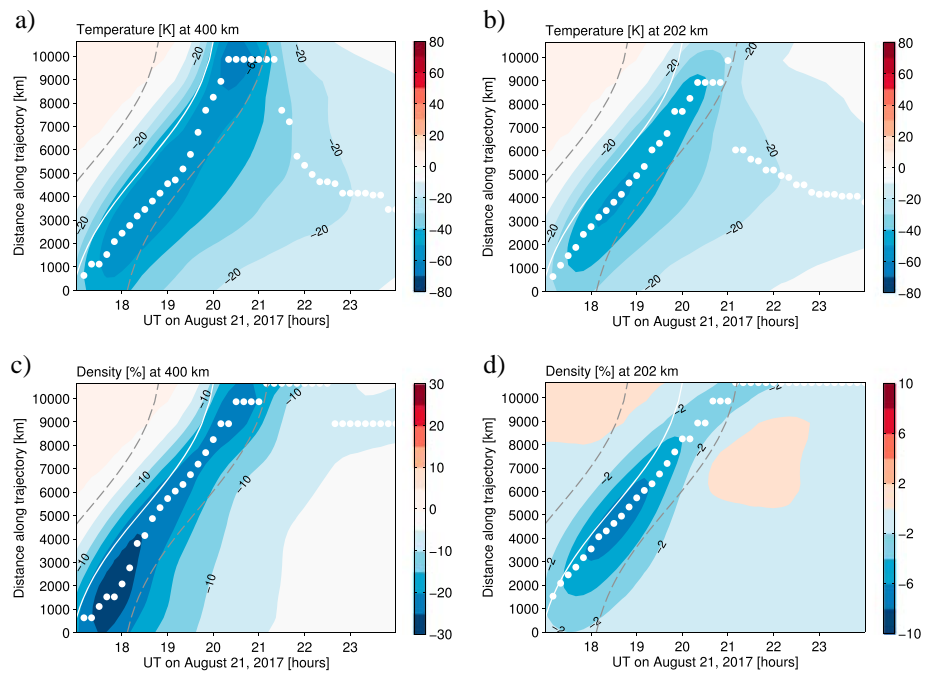
Figure 5. Response of neutral temperature (a, b) and density (c, d) at 400- (left column) and 202-km (right column) altitude along the eclipse trajectory as a function of distance along the trajectory and UT. The white line marks the path of the center of totality, dashed gray lines approximate the edges of the occultation region, and white dots indicate the maximum response of the plotted variable at that time.

in the region with the strongest response is small, the response in $v_{n,par,v}$ is primarily due to the enhanced northward meridional wind, which occurs south and southwest of the eclipse trajectory. Changes in the neutral wind also affect the composition, including the O/N_2 ratio, which is generally a good measure of the balance between ion production and loss processes; a higher O/N_2 ratio is associated with greater electron density. However, when ion production is minimal, as during an eclipse, the atomic oxygen concentration does not matter much, while changes in N_2 density will continue to affect loss rates. During the eclipse the N_2 density decreases (not shown here, but see Wu et al., 2018), which should reduce the loss rate, but this can clearly not balance out the other effects that act to reduce the electron density.

Figures 4a and 4c show zoomed-in maps of the electron temperature and ion temperature responses at 400-km altitude at 19 UT. The electron temperature is strongly reduced in the occultation region, as expected. However, an increase in electron temperature is found to the west of the occultation region, centered at about 27°N, 110°W. This corresponds to the location of the westward extension of the TEC reduction, described above. The lower electron density in this region, combined with being located away from the eclipse path (i.e., little to no reduction in EUV heating), means that the heating rate per electron is higher, which explains the higher electron temperature. A small increase in ion temperature also occurs in the same location, which is probably due to ion-electron collisional heating. Within the occultation region itself the ion temperature is reduced as expected.

The evolution of the response of the thermosphere-ionosphere system, including the lag of the response in various variables with respect to totality, is further investigated in Figures 5–8. These figures show the response of a given variable as a function of time and distance along the eclipse trajectory. At each model time step, parameters are extracted along the eclipse trajectory (i.e., along the white line in Figure 1). The peak response is marked with a white dot every 10 min. The location of totality is shown as a white line, with gray dashed lines marking the approximate start and end of the eclipse. Everything to the right of the white line occurs after totality has reached the point along the trajectory indicated by the vertical axis. The bottom of the vertical axis (distance = 0 km) corresponds to the start point of the eclipse off the northwestern coast of Oregon and the top of the vertical axis (distance = 10,650 km) corresponds to the end point of the eclipse in the Atlantic Ocean.
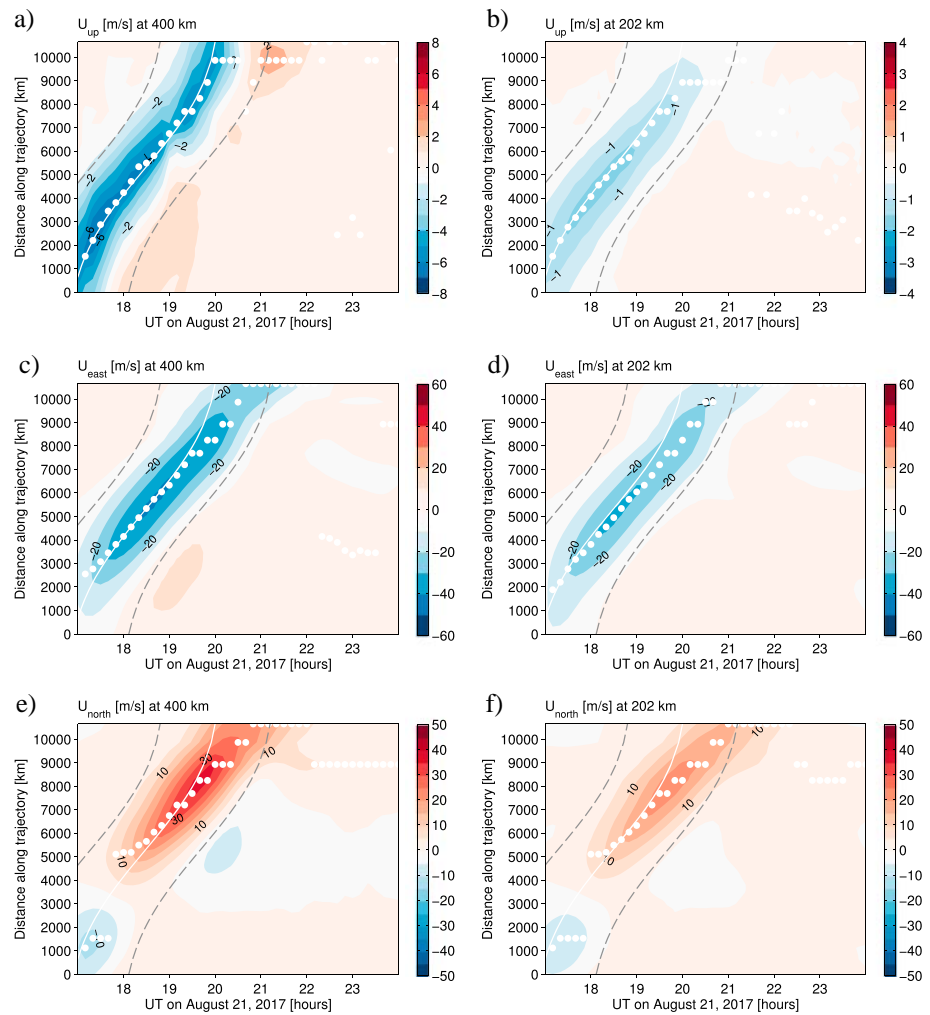
Figure 6. Response of upward wind (a, b), eastward wind (c, d), and northward wind (e, f) at 400- (left column) and 202-km (right column) altitude along the eclipse trajectory as a function of distance along the trajectory and UT. The white line marks the path of the center of totality, dashed gray lines approximate the edges of the occultation region, and white dots indicate the maximum response of the plotted variable at that time.

Figure 5a shows the response of the neutral temperature at 400-km altitude along the eclipse trajectory. The temperature reduction quickly intensifies at the start of the eclipse, until a peak reduction of ∼50 K is reached at 17:30 UT. The peak reduction then remains approximately constant at 50–60 K until 20:00 UT, after which a brief enhancement of the temperature reduction to ∼70 K occurs. It is peculiar that this enhancement occurs just after the total eclipse has ended and it is not clear what is causing it. From about 20:30 UT, the temperature response slowly decays, but a small perturbation persists until the end of the day along most of the eclipse trajectory.

The maximum mass density reduction at 400-km altitude, shown in Figure 5c, is strongest in the beginning of the eclipse, peaking between 17:30 and 18:00 UT at nearly 30%. After this it stabilizes to about 20–25%. However, the temporal evolution of the density response is different when viewed in absolute terms rather than as a percentage, as shown here. In absolute terms (not shown), the peak density response steadily increases throughout the eclipse event, but because the background density is smaller at the start of the eclipse than toward the end (due to a difference in local time), the initial response appears relatively large when presented in percentage terms.

Both the temperature and density responses start to lag behind totality early on in the event, shortly after 17:00 UT. The lag of the peak temperature response stabilizes to ∼ 35 minutes from about 18:00 UT. This is very similar to the 30-min lag found by Müller-Wodarg et al. (1998) in their simulation study of the 11
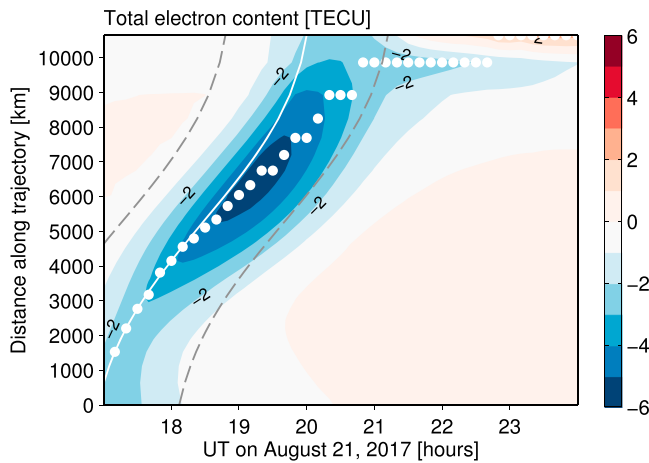
Figure 7. Response of total electron content along the eclipse trajectory as a function of distance along the trajectory and UT. The white line marks the path of the center of totality, dashed gray lines approximate the edges of the occultation region, and white dots indicate the absolute maximum of the plotted variable at that time.

August 1999 eclipse with the Coupled Thermosphere-Ionosphere-Plasmasphere model, and also similar to the lag evident in simulations with the Whole Atmosphere Community Climate Model eXtended of the 21 August 2017 eclipse by McInerney et al. (2018). The peak mass density response follows totality more closely than the peak temperature response for most of the event, between about 18:00 and 20:00 UT, with a lag of around 20 min.

The vertical neutral wind response may play an important role in causing the different lags of the neutral temperature and mass density responses with respect to totality, as discussed above. Its temporal evolution along the eclipse path at 400-km altitude is shown in Figure 6a. A downward vertical wind response leads totality briefly at the start of the eclipse, but closely follows totality from 17:00 UT until the end of the total eclipse. Perturbation winds turn upward ~40 min after totality. A brief strengthening of this upward wind response occurs between 21:00 and 21:30 UT at the end of the eclipse trajectory, which might be related to the temperature reduction enhancement that occurred in the same location a bit earlier.

The eastward and northward wind responses at 400-km altitude are shown in Figures 6c and 6e, respectively. A westward (negative) disturbance wind leads totality until about 17:30 UT, longer than the vertical wind. This is probably because the horizontal wind starts to respond as soon as a horizontal pressure gradient is set up, which can already happen before a (partial) shadow arrives at the location in question, while the vertical pressure gradient that is important for the vertical wind response only starts to develop once the edge of the eclipse arrives. The eastward wind response closely follows totality until about 19:30 UT, after which an increasing lag with respect to totality forms. This might be because the shadow moves too quickly for the wind response to keep up, as they take some time to adjust. The disturbance wind turns eastward ~ 70 minutes after totality, and this is strongest in the early part of the eclipse. The northward wind response is complicated by a sign change,
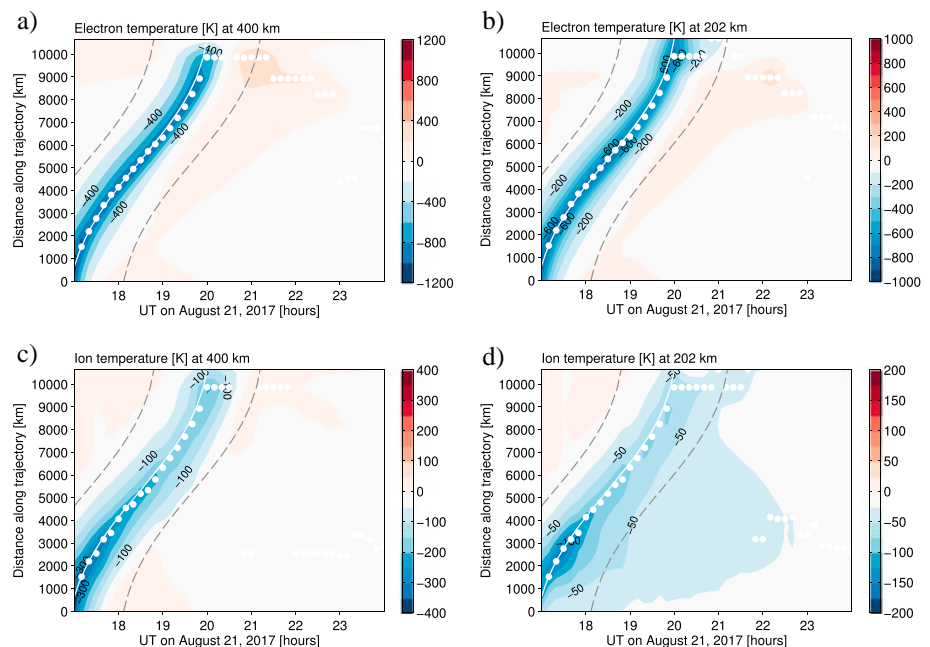

Figure 8. Response of electron temperature (a, b) and ion temperature (c, d) at 400- (left column) and 202-km (right column) altitude along the eclipse trajectory as a function of distance along the trajectory and UT. The white line marks the path of the center of totality, dashed gray lines approximate the edges of the occultation region, and white dots indicate the absolute maximum of the plotted variable at that time.

which is probably related to the orientation of the eclipse trajectory. When the response stays the same sign, the evolution looks similar to that of the eastward wind.

Figure 7 shows the TEC response along the eclipse trajectory. The reduction in TEC follows the path of totality closely from the start of the eclipse until about 18:00 UT, after which a lag forms that increases over time. This suggests again that the system is not able to respond fast enough to keep up with the movement of the shadow.

The electron temperature at 400-km altitude, shown in Figure 8a, decreases by more than 1000 K centered at totality. There is almost no lag with respect to totality, indicating that the electron temperature is close to being in steady state, unlike the neutral temperature. The electron temperature shows a positive response of about 500 K approximately an hour after totality has passed for the second half of the eclipse trajectory. This increase after totality can be explained by the reduction in electron density combined with only a mild decrease in EUV flux, resulting in a higher heating rate per electron. The ion temperature response (Figure 8c) is almost entirely negative and follows the path of totality closely, with only a minor lag forming toward the end of the eclipse. However, the strongest response occurs early on and gradually weakens as the eclipse progresses. This is due to the background ion temperature being higher in the early part of the eclipse trajectory; the reduction in EUV radiation then has a relatively larger effect in absolute terms.

Responses to the eclipse can be expected to vary with altitude. To give an indication of variations with altitude, we will now briefly describe how responses obtained at 400-km altitude compare with those obtained at an altitude of ~200 km. These were shown alongside results for 400-km altitude in Figures 2, 4–6, and 8.

In general, the thermosphere responses are weaker at 202-km altitude. For instance, the maximum neutral temperature and density responses at 202-km altitude are nearly 50 K and nearly 8%, respectively, compared to ~70 K and nearly 30% at 400-km altitude (Figure 2). However, the thermosphere responses are similar in their geographical distribution. Ion and electron temperature responses at 202 km are also weaker but are different in form as well: They do not show the enhancement to the west of the eclipse path that was found at 400-km altitude (Figure 4). This is likely due to differences in the electron density responses at 202- and 400-km altitude: the westward extension of the reduction in TEC, shown in Figure 3a, is present in the electron density response at 400-km altitude, while the electron density response at 202-km altitude exhibits a small enhancement west of the eclipse path (not shown). This is consistent with plasma being transported down along the magnetic field by the neutral wind (Figure 3b), causing a reduction in electron density at 400-km altitude and a small increase at lower altitude west of the eclipse path. At 202-km altitude there is therefore no increase in the heating rate per electron west of the eclipse path, and hence no enhancement in electron or ion temperature in this region.

The evolution of the responses along the eclipse path at 400- and 202-km altitude are mostly very similar. The largest difference appears to be in the neutral density response, which shows a gradually increasing lag with respect to totality at 202-km altitude, which was not found at 400-km altitude (Figure 5). The responses in upward and eastward wind also show this gradually increasing lag to a somewhat greater extent at 202 than at 400-km altitude. This indicates that the response of the thermosphere at 202-km altitude is not able to keep up with the fast-moving shadow as well as the thermosphere at 400-km altitude.

3.2. Comparison to Observations

This section compares the simulation results to observations of the eclipse response to assess how well GITM is able to reproduce these. Since there are more observations available for the ionosphere, these are described first. Wu et al. (2018) already performed comparisons between GITM and measurements of N_MF_2 from several ionosonde stations as well as Global Positioning System (GPS) measurements of TEC. While they used a different EUV flux model, the results obtained here are quite similar, so only one example of the simulated response of TEC in comparison to GPS observations is shown in Figure 9.

The GPS TEC response to the eclipse was obtained by using 29 August 2017 as a reference day, following Coster et al. (2017). Responses are shown both as a percentage difference relative to the reference case (Figure 9a) and in absolute TEC units (Figure 9b) at ~19 UT. When viewed as a percentage difference, the observed and simulated TEC responses agree quite well in terms of peak magnitude, but the observed TEC reduction is relatively strong over a larger area than in the model. When absolute TEC units are used, the simulated response, including the peak response, is weaker than observed. This makes sense, as the model does not include electron content above ~550-km altitude. We further note that the observed TEC reduction
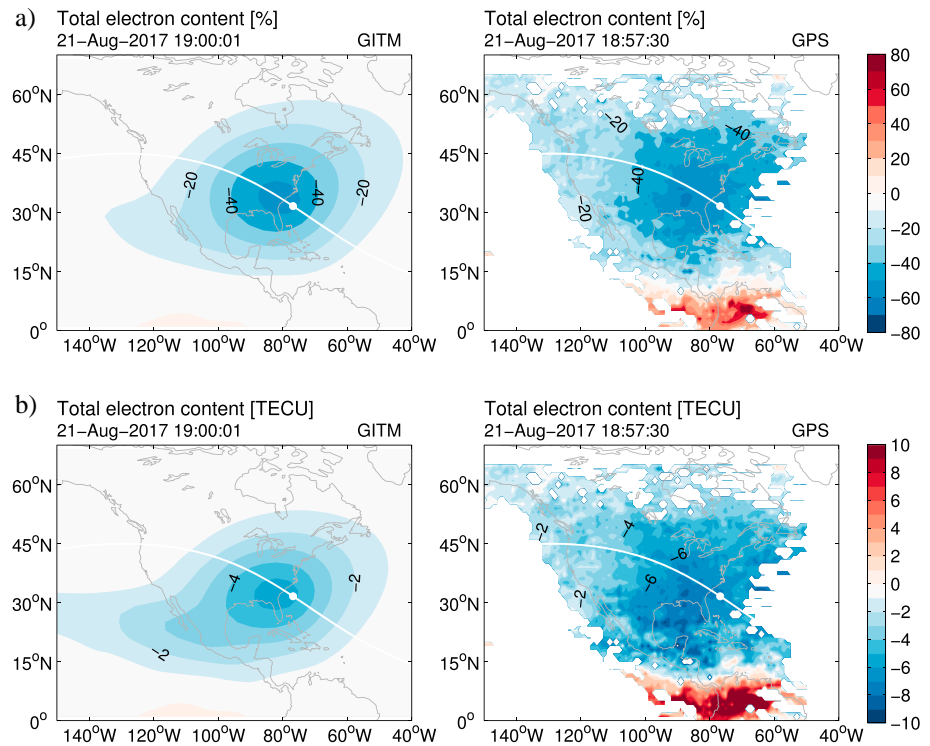
Figure 9. Total electron content response as a percentage (a) and in TEC units (b) for Global Ionosphere Thermosphere Model (left column) and as observed by Global Positioning System (right column) at ~19 UT. The white line marks the path of the center of totality and the white dot indicates its current position.

remains strong well after the eclipse has passed, while the simulated TEC reduction decays much more quickly, as was shown by Wu et al. (2018).

We also compare GITM results with a wider range of ionospheric variables observed by the Incoherent Scatter Radar at Millstone Hill (geographic coordinates: 42.6°N, 71.5°W) as published by Goncharenko et al. (2018). Millstone Hill experienced a partial eclipse starting at 17:27 UT, maximizing at 18:46 UT at nearly 63% obscuration, and ending at 19:59 UT. Figure 10 shows the response in electron density, electron and ion temperature, and vertical drift as simulated by GITM and as observed by the radar. The latter three variables are only shown up to 400-km altitude, as results obtained for higher altitudes are considered less reliable, while electron density is shown up to 550 km altitude. The observed response was obtained using 22 August 2017 as the reference day, following Goncharenko et al. (2018). Note that this is different from the approach taken with the GPS data above, where 29 August 2017 was used as a reference day. There are arguments to be made for either of these days to be the most appropriate (see Coster et al., 2017; Goncharenko et al., 2018), so we follow here the methods used by the experts on the data sets in their respective publications. The reduction in electron density simulated by GITM is ~30% stronger than observed by the radar and also extends over a larger vertical range, but it is reasonable in duration. However, the clearly observed posteclipse enhancement in electron density is much weaker in the model. The reduction in electron temperature simulated by GITM is again considerably stronger than observed, while the reduction in ion temperature is weaker than observed, especially around 150- to 200-km altitude. Both the ion and electron temperatures also show notable differences still after the eclipse in the observations, including an enhancement in the perturbations (both positive and negative) after ~23 UT, while the simulated responses decay quickly after the end of the partial eclipse.

Some of the discrepancies between the simulated and observed perturbations are related to noneclipse effects that can not be eliminated from the observations but are not present in the model simulations, for instance, due to differences in the geophysical conditions between 21 and 22 August 2017. This also explains why there are signatures present in the observations already before the actual start of the partial eclipse: These are differences between 21 and 22 August 2017 that are unrelated to the eclipse. However, we can
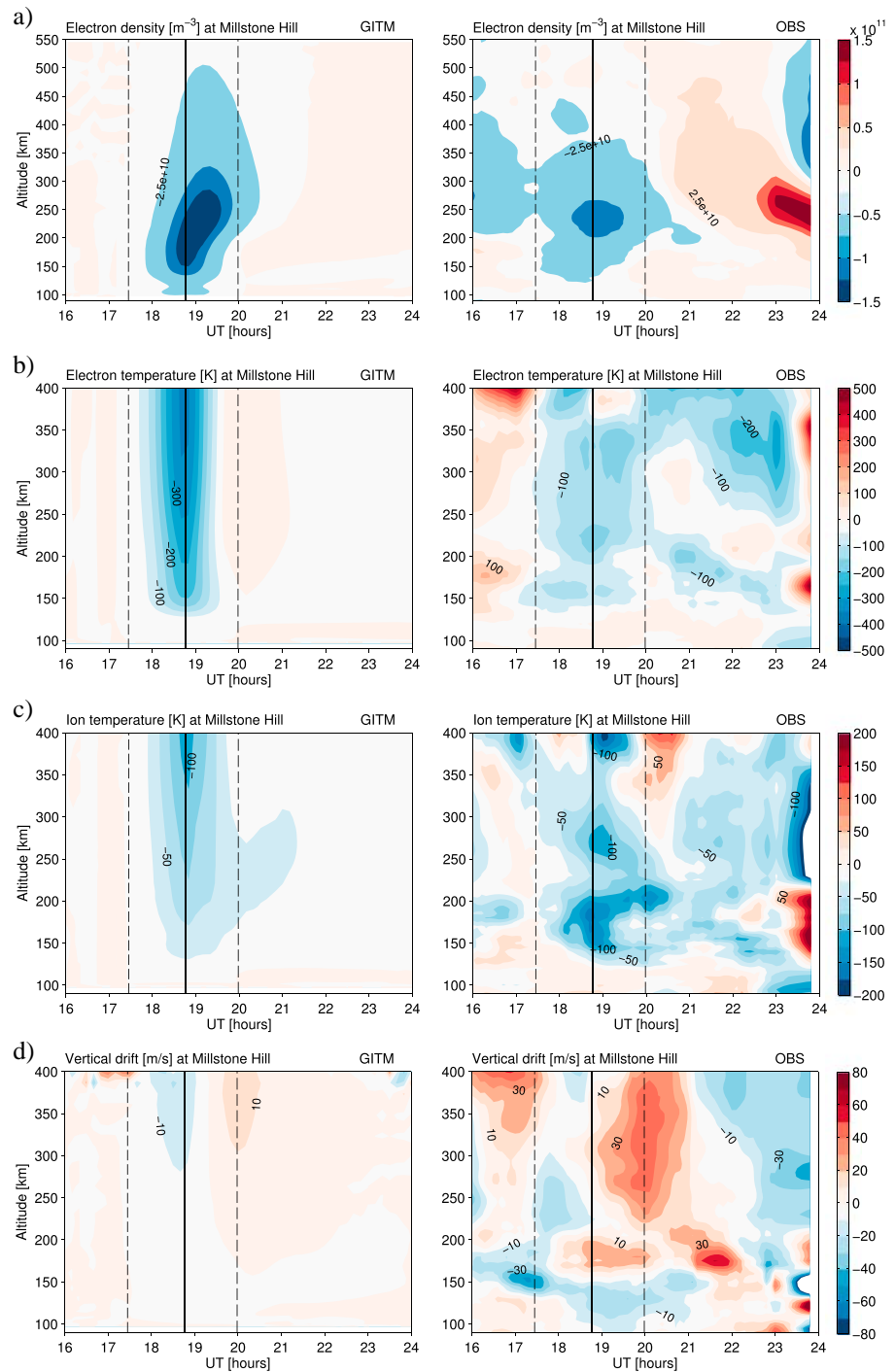
Figure 10. Response in electron density (a), electron temperature (b), ion temperature (c), and vertical drift (d) for GITM (left column) and observed by the Incoherent Scatter Radar at Millstone Hill. The solid black line marks the time of maximum obscuration and the dashed lines mark the start and end of the partial eclipse. GITM = Global Ionosphere Thermosphere Model.
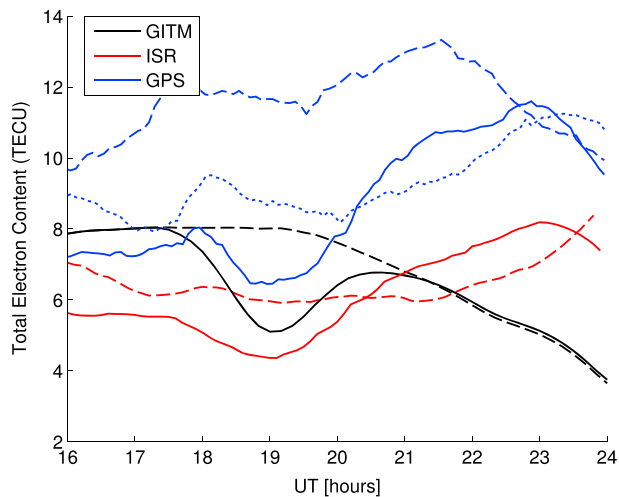
Figure 11. Total electron content at Millstone Hill based on GPS data (blue), radar data up to 550-km altitude (red), and model simulations (black) for the control case (dashed lines) and for the eclipse event (solid lines). The control cases shown in the dashed lines are the same as in Figures 9 and 10 for the respective data sets and therefore correspond to 29 August 2017 for the GPS data and 22 August for the radar data. An additional control case for the GPS-based TEC is shown based on data from 22 August 2017 (blue dotted line). GPS = Global Positioning System; ISR = Incoherent Scatter Radar; GITM = Global Ionosphere Thermosphere Model.

probably not explain all of the discrepancies between the observed and simulated responses in this way. For instance, it seems unlikely that the posteclipse enhancement in the electron density can be explained by noneclipse effects, given that several other studies have reported similar posteclipse effects, both for this eclipse (e.g., Cherniak & Zakharenkova, 2018; Wu et al., 2018) and previous events (e.g., Chen et al., 2013). It is then also reasonable to think that the ion and electron temperature responses that occur around the same time as the posteclipse electron density enhancement are associated with the same posteclipse effect, in particular, the relatively strong signatures seen after 23 UT.

Goncharenko et al. (2018) already commented on the rather interesting upward vertical drift forming toward the end of the partial eclipse at Millstone Hill. GITM also shows an upward vertical drift appearing toward the end of the occultation period, which is in excellent agreement with the observations in terms of timing. However, the vertical drift response in GITM is much weaker than observed, by approximately a factor of 4. The upward plasma drift at the end of the eclipse is thought to supply plasma to the plasmasphere as the ionosphere is recovering from the eclipse, in a similar way as would happen at sunrise (Goncharenko et al., 2018). After 21 UT, the plasma drift is relatively more downward again, feeding plasma to the ionosphere, which can help explain the observed posteclipse enhancement in electron density and changes in plasma temperature. If this hypothesis is correct, it is not surprising that GITM is missing the posteclipse effects, as the model does not include a plasmasphere. Any plasma flowing up from the model domain during the initial eclipse recovery phase is simply lost and cannot come back down again.

Combining the results from the model comparisons with GPS TEC and the radar-based electron density at Millstone Hill, we find that GITM underestimates the observed TEC reduction (Figure 9) but yet overestimates the observed electron density reduction at Millstone Hill (Figure 10a). To resolve this contradiction, Figure 11 makes a direct comparison between the GPS TEC interpolated to Millstone Hill, TEC obtained by vertically integrating the radar-based electron density at Millstone Hill up to 550-km altitude, and the model results (also obtained by integrating the electron density up to ~550-km altitude). This clearly demonstrates the large discrepancy between the GPS-based and radar-based observations, with the model results sitting in between. There are two key differences between the observational data sets that probably explain most of the discrepancy. First, the GPS-based TEC includes electron content from higher altitudes than the radar-based TEC, which only goes up to 550-km altitude. Based on a typical electron density profile, this could explain a difference on the order of around 25% (González-Casado et al., 2015). Second, the control cases for the two observational data sets are based on data from different days (22 August 2017 for the radar data; 29 August 2017 for the GPS data). To assess the effect of this on the results, the GPS-based TEC for 22 August 2017 is also shown in Figure 11 (radar data for 29 August 2017 are not available). This makes the GPS-based TEC indeed more similar to the radar-based TEC for the control case, so it is clear that the difference in control day contributes to the discrepancy between the observational data sets. We note that another study of GPS-based TEC responses to the eclipse by Cherniak and Zakharenkova (2018) used a different reference case from Coster et al. (2017), namely, the mean of 20 and 22 August 2017, and also found generally smaller TEC reductions than Coster et al. (2017). The difference in TEC between 22 and 29 August 2017 is probably due to differences in geomagnetic activity: 18–23 August 2017 was a geomagnetically active period, while conditions were much quieter on 29 August 2017. Given that the simulations cover an altitude range similar to the radar observations, the simulated TEC should be most similar to the radar-based TEC, but it is clearly too large until about 21:00 UT and too small after about 22:00 UT. This suggests that GITM might overestimate the electron density during the day and underestimate it around dusk and nighttime.

There are few thermospheric observations available during the eclipse, and unfortunately, we do not have access to any in the US. However, Harding et al. (2018) recently showed Fabry Perot interferometer observations of the thermospheric wave generated by the eclipse on the nightside near Cariri, northeastern Brazil (geographic coordinates: 7.4°S, 36.5°W) at 250-km altitude. They compared their observations to simulations
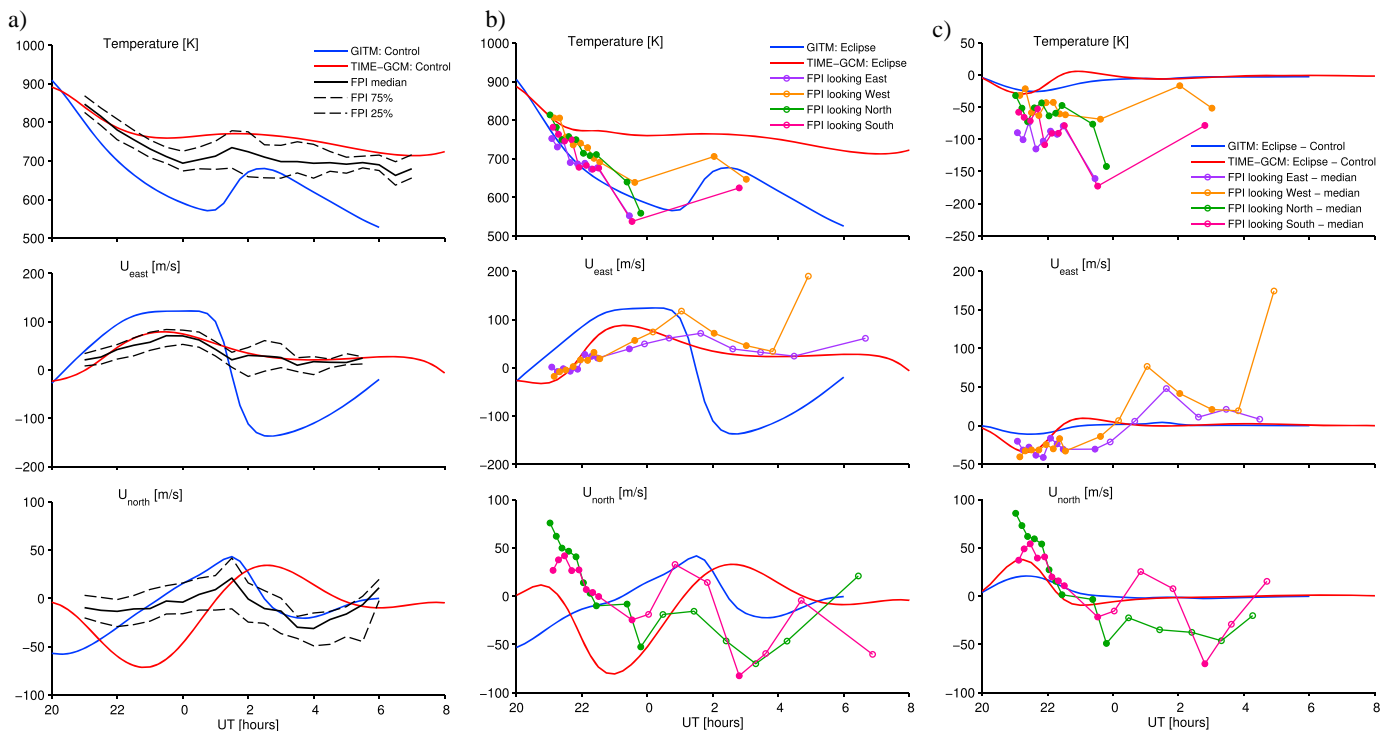
Figure 12. Neutral temperature (top), eastward wind (middle), and northward wind (bottom) for the control case (a), the eclipse event (b), and the difference (c) for GITM, TIME-GCM, and FPI observations from 20:00 UT on 21 August 2017 until 08:00 UT on 22 August 2017. The FPI control case consists of the 30-day median (solid black line), while the 25th and 75th percentiles are also shown for reference (dashed black lines). Measurements on 21–22 August 2017 are shown as multicolored circles (see legend for details); open circles indicate less reliable measurements. GITM = Global Ionosphere Thermosphere Model; TIME-GCM = Thermosphere-Ionosphere-Mesosphere-Electrodynamics General Circulation Model; FPI = Fabry Perot interferometer.

done with the Thermosphere-Ionosphere-Mesosphere-Electrodynamics (TIME)-GCM. The GITM results have been added to this comparison in Figure 12. Background values for the control case are shown in Figure 12a, values for the eclipse event in Figure 12b, and the difference in Figure 12c. The control case for the Fabry Perot interferometer observations consists of median values for the 30-day period starting 20 August 2017 (see Harding et al., 2018, for details). Low airglow brightness during some posteclipse periods precludes a temperature estimate and yields questionable wind estimates, shown with an open circle in Figure 12.

The TIME-GCM captures the observed temperature for the control case fairly well, but not the temperature variation following the eclipse event, while the opposite is true for GITM: GITM is poor at capturing the temperature variation for the control case but matches the observations rather well for the eclipse event. Both models show a much weaker response to the eclipse event than is indicated by the observations. We are not sure why one model would be better at simulating control conditions, while the other is better at simulating posteclipse conditions.

The TIME-GCM reproduces the eastward wind observed at Cariri quite well, both for the control case and the eclipse case, while GITM simulates typically too strong eastward winds for both cases. Despite the strong winds, the response to the eclipse event at Cariri is too weak. This is probably a further indication that the response simulated by GITM decays too quickly—something that was also noted in the TEC response in comparison with GPS data (Wu et al., 2018).

Both models are poor at reproducing observed northward winds for the eclipse event. The TIME-GCM is also rather poor at capturing the observed northward wind for the control case, while GITM does remarkably well with this. Nonetheless, the TIME-GCM, somewhat miraculously, matches the observed response in northward wind at Cariri quite well, and certainly better than GITM. Still, given the poor agreement with observations for both the control and eclipse cases, it is not clear whether this is down to model skill or simply a lucky coincidence.

4. Discussion and Conclusions

GITM captures some of the broad features of the response of the thermosphere-ionosphere system to the 21 August 2017 eclipse. The model simulates expected reductions in neutral temperature and mass density, perturbation neutral winds that respond to changes in the pressure gradient, and reductions in electron density, and ion and electron temperature. The model simulations help to elucidate the mechanisms responsible for some of the features in the observations.

We have demonstrated the influence of the horizontal neutral wind on the equatorward and westward extension of the TEC response via upward plasma transport along the magnetic field, with additional consequences for ion and electron temperatures. Changes in both the horizontal and vertical wind can also modify the lags of the neutral temperature and mass density responses with respect to totality in slightly different ways. Furthermore, the presence of a lag in the neutral temperature response indicates an imbalance between heating and cooling processes during the eclipse, that is, the neutral temperature is not in steady state, while the electron temperature response shows nearly no lag, indicating it is close to steady state. Further comparison with other models, for example, the TIME-GCM, and ideally, observations, is needed to test whether this behavior is realistic or not. We do not have a ready explanation for the strengthening of the temperature response at the very end of the eclipse and the enhancement in the upward wind response shortly after, as shown in Figures 5 and 6. We speculate that it could perhaps be related to an interaction with the approach of the solar terminator, but it is not clear exactly how this would work.

Comparisons with observations indicate several model deficiencies that we must try to understand in order to make model improvements. First, there are issues with the magnitude of the simulated responses. The simulated reductions in electron density and electron temperature at Millstone Hill appear to be too large, while the simulated responses in ion temperature and vertical drift at Millstone Hill are too weak (Figure 10). Posteclipse effects observed at Millstone Hill are mostly not captured well by the model. The simulated response in TEC appears to be too weak compared to GPS-based measurements (Figure 9), but this could be explained by the difference in altitude range and the choice of control day. Nonetheless, Wu et al. (2018) noted that the simulated TEC response also decays too quickly, and the very small effects on neutral temperature and winds simulated at Cariri in the hours after the event (Figure 12) could be another sign of a lack of persistence in the model response.

We suspect that the lack of persistence in the model response could be related to two things. First, it appears that the heating mechanisms in GITM might be too strong compared to the cooling mechanisms. This would make the thermosphere-ionosphere system recover too quickly after the eclipse event and could also potentially explain rather large contrasts between day and night in mass density compared to Swarm observations (not shown). We need to explore how the heating in GITM might be reduced, while still remaining within known constraints for the relevant parameters. Second, electron densities at middle and low latitudes are too high in the model. Perlongo et al. (2018) showed that this is partly related to a very large O/N_2 ratio, in particular at low latitudes. The high electron density results in too much ion drag on the neutral winds, which is likely to damp the neutral wind response too much. Given the important role of the neutral winds in modifying the TEC response, as well as additional effects on the neutral temperature and mass density responses, this could also result in the ionosphere-thermosphere system as a whole showing too little remaining effects in the hours after the eclipse. It is less clear why some of the initial responses during the eclipse event itself are also too small (and of course this will also contribute to a too small response later on). We plan to follow this up in a future study through a series of additional experiments with GITM as well as a detailed comparison with TIE-GCM and TIME-GCM in the hope that this will shed further light on the issue. The TIE-GCM simulations by Dang et al. (2018) and also Lei et al. (2018) showed a much more persistent eclipse response than our GITM simulations, indicating that it is possible to capture this with an ionosphere-thermosphere model, but inclusion of the middle atmosphere (as in TIME-GCM) could also be important, as the response in this part of the atmosphere is likely to affect the thermosphere and ionosphere response as well (e.g., McInerney et al., 2018). A second important discrepancy between the model and observations is the lack of a posteclipse electron density enhancement, downward vertical drift and signatures in ion and electron temperature at Millstone Hill after 23 UT (Figure 10). The fact that GITM misses these posteclipse effects is consistent with the hypothesis that they are associated with storage of plasma in the plasmasphere at the end of the eclipse, which then flows back into the ionosphere in the hours afterward. Since GITM does not

include a plasmasphere it cannot be expected to capture these effects. However, to confirm this hypothesis it must be tested more thoroughly with a model that does include the plasmasphere.

It was not possible to test the simulated temporal evolution of the global response to the eclipse in detail, other than finding that it decays too quickly, as more observations would be needed to obtain a more detailed picture. We tried creating a figure similar to Figure 7 based on GPS TEC data, but unfortunately, there is insufficient data coverage over the second half of the eclipse trajectory to test whether the simulated lag in the TEC response is realistic or not. We also attempted to find a neutral density response in Swarm satellite data, but unfortunately, the currently available data are too noisy to extract a signal with confidence. Hopefully new missions such as the Global Observations of the Limb And Disk and Ionospheric Connection Explorer will offer more opportunities for model-observations comparisons during future solar eclipses, so that the temporal evolution of the response of the thermosphere-ionosphere system to a total solar eclipse can be investigated in greater detail.

References

Bilitza, D., Altadill, D., Zhang, Y., Mertens, C., Truhlik, V., Richards, P., et al. (2014). The International Reference Ionosphere 2012 – a model of international collaboration. *Journal of Space Weather and Space Climate*, *4*, A07. https://doi.org/10.1051/swsc/2014004

Chamberlin, P. C., Woods, T. N., & Eparvier, F. G. (2007). Flare Irradiance Spectral Model (FISM): Daily component algorithms and results. *Space Weather*, *5*, S07005. https://doi.org/10.1029/2007SW000316

Chen, G., Qi, H., Ning, B., Zhao, Z., Yao, M., Deng, Z., et al. (2013). Nighttime ionospheric enhancements induced by the occurrence of an evening solar eclipse. *Journal of Geophysical Research: Space Physics*, *118*, 6588–6596. https://doi.org/10.1002/jgra.50551

Cherniak, I., & Zakharenkova, I. (2018). Ionospheric total electron content response to the Great American solar eclipse of 21 August 2017. *Geophysical Research Letters*, *45*, 1199–1208. https://doi.org/10.1002/2017GL075989

Coster, A. J., Goncharenko, L., Zhang, S.-R., Erickson, P. J., Rideout, W., & Vierinen, J. (2017). GNSS observations of ionospheric variations during the 21 August 2017 solar eclipse. *Geophysical Research Letters*, *44*, 12,041–12,048. https://doi.org/10.1002/2017gl075774

Dang, T., Lei, J., Wang, W., Zhang, B., Burns, A., Le, H., et al. (2018). Global responses of the Coupled Thermosphere and Ionosphere System to the August 2017 Great American solar eclipse. *Journal of Geophysical Research: Space Physics*, *123*, 7040–7050. https://doi.org/ 10.1029/2018ja025566

Drob, D. P., Emmert, J. T., Meriwether, J. W., Makela, J. J., Doornbos, E., Conde, M., et al. (2015). An update to the Horizontal Wind Model (HWM): The quiet time thermosphere. *Earth and Space Science*, *2*, 301–319. https://doi.org/10.1002/2014EA000089

Goncharenko, L. P., Erickson, P. J., Zhang, S.-R., Galkin, I., Coster, A. J., & Jonah, O. F. (2018). Ionospheric response to the solar eclipse of 21 August 2017 in Millstone Hill (42N) observations. *Geophysical Research Letters*, *45*, 4601–4609. https://doi.org/10.1029/2018GL077334

González-Casado, G., Juan, J. M., Sanz, J., Rovira-Garcia, A., & Aragon-Angel, A. (2015). Ionospheric and plasmaspheric electron contents inferred from radio occultations and global ionospheric maps. *Journal of Geophysical Research: Space Physics*, *120*, 5983–5997. https:// doi.org/10.1002/2014JA020807

Harding, B. J., Drob, D. P., Buriti, R. A., & Makela, J. J. (2018). Nightside detection of a large-scale thermospheric wave generated by a solar eclipse. *Geophysical Research Letters*, *45*, 3366–3373. https://doi.org/10.1002/2018GL077015

Huba, J. D., & Drob, D. (2017). SAMI3 prediction of the impact of the 21 August 2017 total solar eclipse on the ionosphere/plasmasphere system. *Geophysical Research Letters*, *44*, 5928–5935. https://doi.org/10.1002/2017GL073549

Lei, J., Dang, T., Wang, W., Burns, A., Zhang, B., & Le, H. (2018). Long-lasting response of the global thermosphere and ionosphere to the 21 August 2017 solar eclipse. *Journal of Geophysical Research: Space Physics*, *123*, 4309–4316. https://doi.org/10.1029/2018JA025460

McInerney, J. M., Marsh, D. R., Liu, H.-L., Solomon, S. C., Conley, A. J., & Drob, D. P. (2018). Simulation of the 21 August 2017 solar eclipse using the Whole Atmosphere Community Climate Model-eXtended. *Geophysical Research Letters*, *45*, 3793–3800. https://doi.org/10.1029/2018GL077723

Müller-Wodarg, I. C. F., Aylward, A. D., & Lockwood, M. (1998). Effects of a mid-latitude solar eclipse on the thermosphere and ionosphere—A modelling study. *Geophysical Research Letters*, *25*(20), 3787–3790. https://doi.org/10.1029/1998GL900045

Newell, P. T., Sotirelis, T., & Wing, S. (2009). Diffuse, monoenergetic, and broadband aurora: The global precipitation budget. *Journal of Geophysical Research*, *114*, A09207. https://doi.org/10.1029/2009JA014326

Perlongo, N. J., Ridley, A. J., Cnossen, I., & Wu, C. (2018). A year-long comparison of GPS TEC and global ionosphere-thermosphere models. *Journal of Geophysical Research: Space Physics*, *123*, 1410–1428. https://doi.org/10.1002/2017JA024411

Picone, J. M., Hedin, A. E., Drob, D. P., & Aikin, A. C. (2002). NRLMSISE-00 empirical model of the atmosphere: Statistical comparisons and scientific issues. *Journal of Geophysical Research*, *107*(A12), 1468. https://doi.org/10.1029/2002JA009430

Ridley, A. J., Deng, Y., & Tóth, G. (2006). The global ionosphere–thermosphere model. *Journal of Atmospheric and Solar-Terrestrial Physics*, *68*(8), 839–864. https://doi.org/10.1016/j.jastp.2006.01.008

Stone, E. C., Frandsen, A. M., Mewaldt, R. A., Christian, E. R., Margolies, D., Ormes, J. F., & Snow, F. (1998). The advanced composition explorer. *Space Science Reviews*, *86*(1/4), 1–22. https://doi.org/10.1023/a:1005082526237

Wang, W., Dang, T., Lei, J., Zhang, S., Zhang, B., & Burns, A. (2019). Physical processes driving the response of the F2 region ionosphere to the 21 August 2017 solar eclipse at Millstone Hill. *Journal of Geophysical Research: Space Physics*, *124*, 2978–2991. https://doi.org/10.1029/2018JA025479

Weimer, D. R. (2005). Improved ionospheric electrodynamic models and application to calculating joule heating rates. *Journal of Geophysical Research*, *110*, A05306. https://doi.org/10.1029/2004JA010884

Wu, C., Ridley, A. J., Goncharenko, L., & Chen, G. (2018). GITM-data comparisons of the depletion and enhancement during the 2017 solar eclipse. *Geophysical Research Letters*, *45*, 3319–3327. https://doi.org/10.1002/2018GL077409

Zhu, J., Ridley, A. J., & Deng, Y. (2016). Simulating electron and ion temperature in a global ionosphere thermosphere model: Validation and modeling an idealized substorm. *Journal of Atmospheric and Solar-Terrestrial Physics*, *138*, 243–260. https://doi.org/10.1016/j.jastp.2016.01.005